Article

Magnetic Nanoparticles Coated with (*R*)-9-Acetoxystearic Acid for Biomedical Applications

Gabriele Micheletti, Carla Boga,* Dario Telese, Maria Cristina Cassani, Elisa Boanini, Patrizia Nitti, Barbara Ballarin, Alberto Ghirri, Gianni Barucca, and Daniele Rinaldi*

Read Online

ACCESS | Metrics & More | Article Recommendations | Supporting Information

ABSTRACT: The well-known ability to selectively drive nano-magnetic materials coated with anticancer drugs into tumor cells suggested the synthesis and the characterization of magnetic nanoparticles (MNPs) functionalized with (*R*)-9-acetoxystearic acid, the acetic ester of (*R*)-9-hydroxystearic acid (9-HSA), an antiproliferative agent active against different cancer cells. The acyl chloride of (*R*)-9-acetoxystearic acid, synthesized in two steps from 9-HSA, was reacted with (3-aminopropyl)triethoxysilane, chosen as a linker between MNPs and the stearyl moiety. In the last step, the novel amide was bound to magnetite NPs by reaction with silyl groups. A detailed structural, chemical, and magnetic characterization of the obtained material proved that it possesses properties in agreement with the requirements for drug delivery, opening the possibility to further insights focused on the 9-HSA biomedical applications.
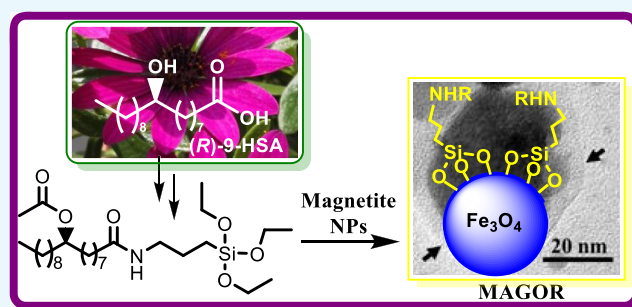
1. INTRODUCTION

The growing interest in magnetic nanoparticles (MNPs) is mainly due to their versatility in a wide number of applicative fields, such as removal of toxic elements from industrial wastes,[1−3] magnetic resonance imaging (MRI) techniques for cancer diagnosis, and cancer therapy.[4−8] Integration of imaging-diagnostic systems based on positron emission tomography (PET) and MRI in a single diagnostic device PET/MRI (up to now the more advanced medical diagnostic instrumentation) moreover requires an effort on advanced material, instrumentation studies, and quality control.[9−12] The main advantage of using MNPs in biomedical field is due to the possibility to guide the drug to the target by means of an external magnetic field. In this context, particular interest is on nanometer-sized particles of iron oxide that allow combination of cancer therapy with their *in vivo* degradation into non-toxic iron ions.[7] MNPs showing superparamagnetic (SPM) behavior have indeed demonstrated their potential in anticancer drug delivery.[13−18]

Magnetite (Fe_3O_4) is a promising candidate as drug delivery medium owing to low toxicity and biocompatibility. The preparation of magnetite, aiming the drug release to the target, is a challenging task as different parameters to control are involved, including the size optimization and surface properties. Low toxicity and the capability to reach the target are connected with the MNP dimension. In fact, too small particles with diameter lower than 10 nm are, most of the time, rapidly removed from the body. On the other hand, particles larger than 200 nm are retained by the spleen. The optimal dimension to fulfill the therapy requirements ranges between 10 and 100 nm.[19−22]

The need to control the MNPs by magnetic fields requires that they be in a SPM state. In the range 10−100 nm, the magnetite is often monodomain,[23] so it behaves as a SPM material as a function of temperature, size, and magnetic interactions. For drug delivery, the SPM behavior is significant at room temperature, and this, requires to control dimensions, magnetic interactions, and size distribution of the MNPs. In addition, the functionalization can modify the magnetic behavior. The coating of MNPs with a drug, for example, can decrease particle interactions and agglomeration, modifying SPM behavior in the whole. MNPs can be derivatized by coating the iron oxide core surface with organic or inorganic molecules through a chemical bond thus obtaining magnetically controlled drug carrier for locoregional cancer treatment.

9-Hydroxystearic acid (9-HSA) is an endogenous cellular lipid able to inhibit the cell growth in a series of cancer cell lines. It has been demonstrated that it acts as an inhibitor of HDAC1 activity at micromolar concentrations; in HT29,

human colorectal adenocarcinoma cells, the inhibitory effect of 9-HSA is mediated by an arrest in the G0/G1 phase cell cycle.[24,25] Molecular docking studies have shown a favorable formation energy of the HDAC1–9-HSA complex, and the complex with (R)-9-HSA became more stable than that with the opposite enantiomer.[26] This prediction was fulfilled after separately administering of both enantiomers.[27] Despite a clinical advantage, the use of (R)-9-HSA shows some limitations, such as the extremely poor water solubility and the need to administer relatively high doses in order to have a pharmacological effect. Recently, we focused our efforts on the search of efficient delivering modes of (R)-9-HSA, and we were able to load it in biocompatible keratin nanoparticles[28] and to insert it in hydroxyapatite nanocrystals[29,30] for possible applications in bone cancer. Now, in order to find a more general and versatile method to target the action of (R)-9-HSA toward local treatment sites and considering that the anchoring amido group, as well as the ester group, may be "in situ" hydrolyzed by cellular lipases and amidases thus permitting the release of the organic molecule, we planned to coat (R)-9-HSA to MNPs through (3-aminopropyl)triethoxysilane $(NH_2(CH_2)_3Si(OC_2H_5)_3$ (APTES), known for its ability to combine with biomolecules, drugs, and metals.[31] In the present study, we report the synthesis and a detailed structural, magnetic, and chemical characterization of this novel material.

2. RESULTS AND DISCUSSION

2.1. Magnetite Nanoparticles Preparation and Functionalization.
The synthetic strategy designed to functionalize magnetite nanoparticles with (R)-9-HSA implied his connection to APTES through an amide bond, followed by the anchoring to magnetite exploiting the reaction between the silyl group of the obtained amide and the magnetite hydroxy groups. A well-known and efficient synthetic route to amides is the reaction between an amine and an acyl chloride; in current case, taking into account the presence, on the (R)-9-HSA, of a hydroxy- and a carboxy-functionality, the hydroxy group needed to be protected prior the formation of the acyl chloride, to avoid the occurrence of undesired reactions. The synthetic sequence is shown in Scheme 1.

(R)-9-HSA (1) was enzymatically transformed into (R)-9-acetyl-HSA (2) and then treated with oxalyl chloride to produce the corresponding acyl chloride 3. The latter was reacted with APTES under Schotten–Baumann type conditions[32] to give the amide 4. The reactions (and related work-up procedures) of the second and third step (shown in Scheme

Scheme 1. Synthesis of Amide 4 from APTES and (R) 9-Hydroxystearic Acid
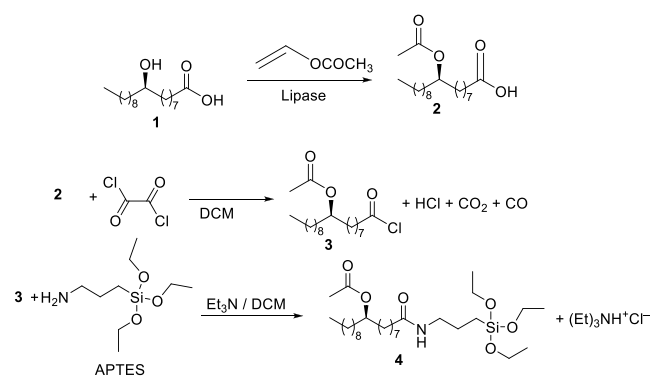
1) have been carried out under inert atmosphere, to avoid hydrolysis, and compounds 3 and 4 were used without purification.

It has to be noted that the usually reported way to coat MNPs with an organic moiety through APTES bridge is realized by reacting MNPs with APTES and then by linking the organic moiety to the amino group of APTES-coated MNPs. In the current case, we first prepared the amide 4 between APTES and (R)-9-acetoxystearic acid by monitoring the reaction course through ^{1}H NMR spectroscopy (Supporting Information file, Figures S1–S6). Once the reaction resulted to be complete, we reacted the crude 4 with magnetite nanoparticles (B-magnetite), in turn prepared via co-precipitation of iron sulphate salts in basic media.[33] The material was washed with anhydrous toluene to remove the eventually unreacted organic compound 4. The functionalization of magnetite nanoparticles with compound 4 must be carried out under strictly anhydrous conditions to avoid secondary hydrolysis of 4 by traces of water prior its bonding with magnetite nanoparticles with consequent formation of undesired byproducts. For this reason, we chose anhydrous toluene as solvent because other possible polar non protic solvents, such as DMSO or DMF, are afflicted by high hygroscopicity and/or high boiling point that make their complete removal difficult.

The IR spectrum of the novel final material was compared with that of B-magnetite (see spectra in Supporting Information, Figure S7) and showed bands at 2927.7 cm^{-1} because of aliphatic CH bonds, 1735.2 and 1031.7 cm^{-1} belonging to the ester group, and 1659.8 cm^{-1}, typical of the amide group, thus confirming the successful derivatization with the organic compound 4. The novel material was indicated as MAGOR (Scheme 2).

2.2. X-ray Diffraction Measurements.
The X-ray diffraction (XRD) patterns of B-magnetite and MAGOR are reported in Figure 1. In particular, diffraction peaks of Figure 1a can be attributed to the magnetite (Fe_3O_4) phase ("International Centre for Diffraction Data"—ICDD card no. 19-0629); but because of very similar XRD patterns, the presence of the maghemite (γ-Fe_2O_3) phase cannot be excluded (ICDD card no. 39-1346).[34] Direct comparison between diffraction patterns of Figure 1a,b shows that MAGOR is composed of the same crystalline phase detected in B-magnetite. Furthermore, no significant variation indicating the presence of amorphous material or reflection broadening is observed, suggesting that the crystallinity of starting iron oxides is maintained after the functionalization with the organic moiety. The mean dimension of the crystalline domains was calculated by the Scherrer equation applied to the XRD patterns. The same value of ~17 nm was obtained for B-magnetite and MAGOR inside the experimental error.

For quantification of the organic material associated to inorganic magnetite in MAGOR, thermogravimetric (TGA) analyses were performed both on B-magnetite and on MAGOR. The two thermogravimetric profiles differ because of complete decomposition of the organic moiety between 150 and 600 °C (Figure 2). Evaluation of the difference between the total weight loss of MAGOR and that of B-magnetite allows us to determine organic moiety content, which amounts to ~9 wt %.

2.3. Transmission Electron Microscopy Observations.
Transmission electron microscopy (TEM) observations were performed to further investigate the MNP structure. Both B-

Scheme 2. Sketch of the Procedure Adopted in Current Work for the Synthesis of MAGOR
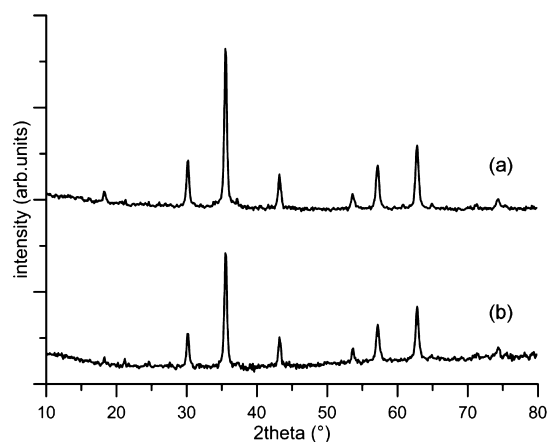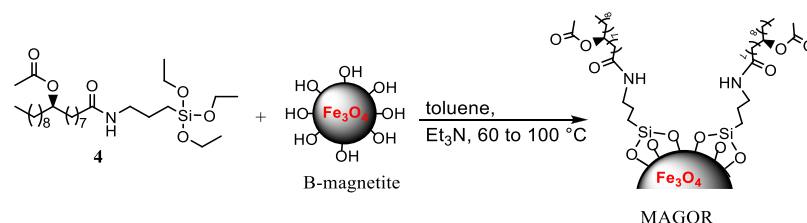

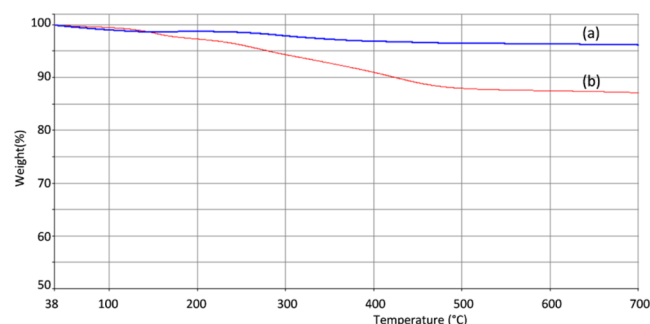**Figure 1.** XRD patterns of (a) B-magnetite and (b) MAGOR nanoparticles.

Figure 2. TGA plots of (a) bare nanoparticles (B-magnetite) and (b) coated nanoparticles (MAGOR).

Figure 3. (a–d) TEM analysis: (a) general view of B-magnetite nanoparticles; (b) corresponding SAED pattern; (c) high-resolution image of a B-magnetite nanoparticle; and (d) high-resolution image of a MAGOR nanoparticle.

magnetite and functionalized MAGOR were investigated. In particular, Figure 3a shows a general view of B-magnetite. The MNPs appear widely size-distributed and disorderly arranged on the carbon film of the TEM grid. The shape of the particles is approximately spherical with diameter ranging from 10 to 40 nm. It must be stressed that although the particle size is inhomogeneous, their diameters are fully comprised inside the interval recommended for drug delivery particles (between 10 and 100 nm). Selected area electron diffraction (SAED) measurements were performed to investigate the crystallinity and composition of the MNPs. Figure 3b is the SAED pattern of the particles visible in Figure 3a. It is composed of well-defined diffraction rings which indicate the random orientation of the particles and their good crystallinity degree. The diffraction rings in the SAED pattern correspond to the following interplanar distances: $d_1 = (0.483 \pm 0.003)$ nm, $d_2 = (0.296 \pm 0.003)$ nm, $d_3 = (0.253 \pm 0.002)$ nm, $d_4 = (0.210 \pm 0.002)$ nm, $d_5 = (0.171 \pm 0.002)$ nm, $d_6 = (0.161 \pm 0.001)$ nm, and $d_7 = (0.149 \pm 0.001)$ nm. These values are in good
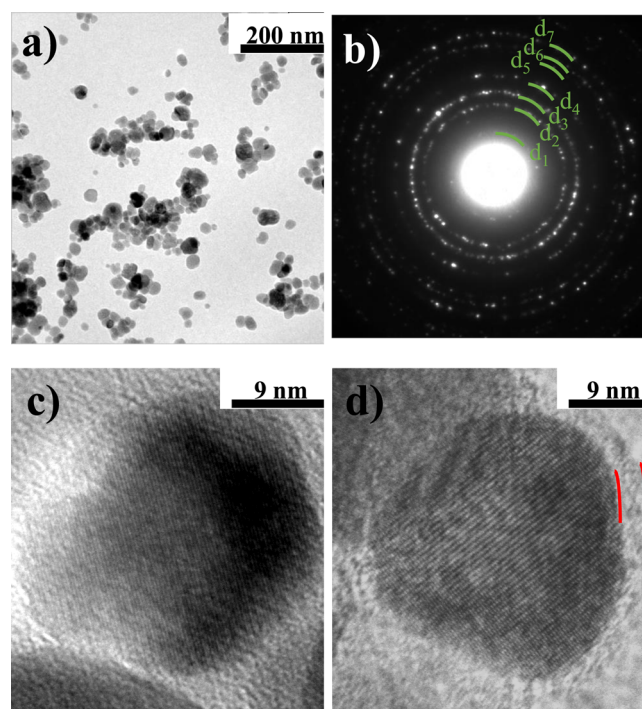
agreement with diffraction data reported for magnetite/maghemite (ICDD card no. 19-0629/ICDD card no. 39-1346: $d_1(111)$; $d_2(220)$; $d_3(311)$; $d_4(400)$; $d_5(422)$; $d_6(511)$, and $d_7(440)$). It is important to stress that no other phases were detected by SAED measurements performed on other groups of particles, and the same results, just reported, were also found for MAGOR, indicating that the upload of the organic material does not influence size, composition, and crystallinity of the MNPs.

High-resolution TEM (HRTEM) observations reveal that the MNPs are single crystals and so the mean dimension of crystalline domains obtained by XRD (~17 nm) coincides with the average size of the MNPs. In particular, Figure 3c,d shows the inner structure of two typical nanoparticles. The atomic planes are clearly visible and extend with continuity from one side to the other of the particles. In more detail, Figure 3c shows an as-built MNP, while Figure 3d shows an MNP covered with the organic moiety (MAGOR). Actually, looking at the exterior of this last nanoparticle, it is possible to observe an amorphous layer (red lines) that can be associated to the organic coating of the particle surface. The same layer is not revealed on the as-built MNP surface, and the visible "orange peel" contrast at the exterior of the particle of Figure
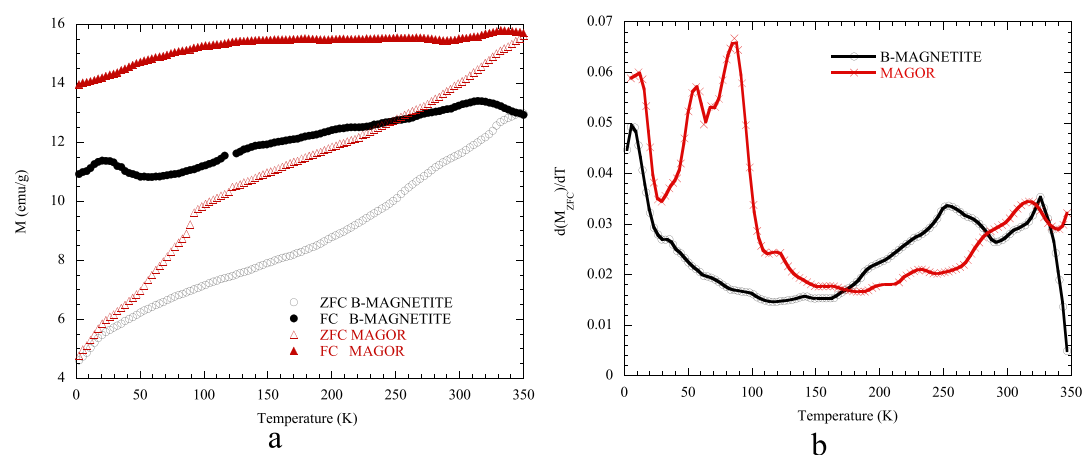
Figure 4. (a) ZFC and FC curves for the B-magnetite and MAGOR samples. Empty symbols are ZFC and the filled symbols are FC. (b) Derivative $d(M_{ZFC})/dT$ for the B-magnetite and MAGOR samples.
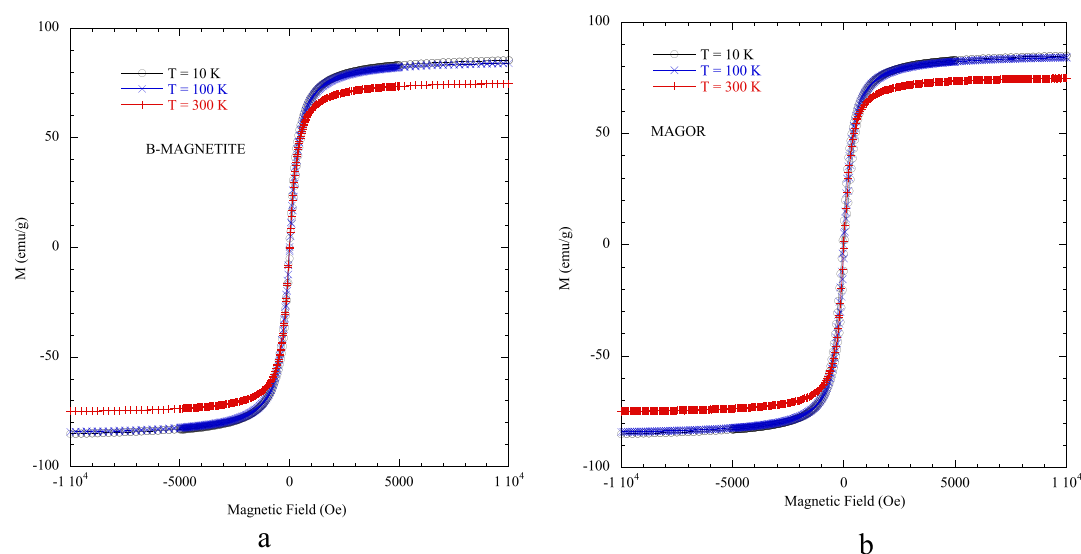

Figure 5. (a) Hysteresis loops for B-magnetite. Measurements are taken at different temperatures. (b) Hysteresis loops for MAGOR. Measurements are taken at different temperatures.

3c is due to the amorphous carbon film over the TEM grid. TEM observations performed on other MAGOR nanoparticles always reveal the presence of a quite uniform amorphous layer on them, suggesting a homogeneous distribution of the organic coating around the nanoparticles (Figure S8 in Supporting Information).

2.4. Magnetic Measurements. MNP structures and size (d) play a significant role in determine their magnetic behavior. In particular, XRD and TEM analyses reveal that "d" ranges from 10 to 40 nm, with an average value of about 17 nm. These values are well below the limit for the magnetite magnetic monodomain dimension (*i.e.*, often $d \approx 100$ nm), suggesting that each nanoparticle is a single magnetic domain.[35,36] Zero-field cooled (ZFC) and field cooled (FC) curves show complex behavior because of the particle size distribution (Figure 4a). The mean blocking temperature is established over 350 K for both samples. In the low temperature regime, a rapid slope variation is detectable. The kink at about 20 K in both samples can be due to a spin glass (SG) like behavior. The phenomenon responsible of the SG like behavior can be identified into the dipolar interactions because the grain surface appears quite ordered, as revealed by

HRTEM observations. However, this does not completely exclude surface-core spin interaction because of magnetic energy minimization.[37,38] For the MAGOR sample, it is possible to detect a second kink at about 90 K. This can be the signature of a Verwey transition, which is not detectable in B-magnetite NPs (Figure 4a). The differences between the two samples can be ascribed to the organic functionalization of the MAGOR NPs surface, which slightly modifies the surface and increases the interparticle distance, thus decreasing their mutual interactions.

More insight can be extracted from the derivative $d(M_{ZFC})/dT$ plot shown in Figure 4b. A peak at low temperature (about 10−20 K) is present in both samples. This confirms the presence of a SG like transition which can be ascribed to the collective behavior because of dipolar coupling between different particles.[39] Moreover, at about 80−90 K, in MAGOR sample, a possibly Verwey transition can be detected. The Verwey transition was reported in literature to be observed even for $d < 50$ nm at about $T_v = 90$ K. In fact, the increased surface/volume ratio can modify the Fe^{2+}/Fe^{3+} ratio through partial oxidation inducing a decreasing of the bulk transition temperature $T_v = 120$ K.[39] B-magnetite does

not present evidence of Verwey transition which, in this sample, can be hindered by dipolar interactions. $d(M_{ZFC})/dT$ measurements confirm the behavior outlined by ZFC−FC, putting in evidence a slight difference at low temperatures because of the organic materials at the surface. The observed small differences are due to the fact that the particles are relatively large to observe a significant coating effect. At higher temperatures, there is a distribution of blocking temperature (T_B) because of the size dispersion. In fact, the temperature T_B is a function of the particle volume and can be valued by eq 1[40]

$$T_B = \frac{E_A}{25k_B} = \frac{KV}{25k_B} \tag{1}$$

where E_A is the barrier energy, K is the anisotropy constant, V the volume, and k_B the Boltzmann constant. For $T > T_B$ the particle is "unblocked", that is, the thermal energy will overcome the anisotropy energy (E_A), so the magnetization direction of the particle begins to fluctuate in the direction allowed by the easy axis. From the FC−ZFC measurements, the irreversibility is reached over 350 K, so to better understand the magnetic behavior, especially at high temperature, it is necessary to evaluate the hysteresis loops for both the samples. In Figure 5a,b are plotted the loops at different temperatures.

The saturation magnetization for both B-magnetite and MAGOR samples is reported in Table 1. Ms has been obtained extrapolating the magnetization measurements at the limit $(1/H) \rightarrow 0$ by[39,41]

$$M = M_s\left(1 - \frac{A}{H} - \frac{B}{H^2}\right) \tag{2}$$

Table 1. Magnetization Saturation M_s for B-Magnetite and MAGOR at Different Temperatures

sample	temperature (K)	M_s (emu/g)
B-magnetite	10	87.9 ± 0.9
MAGOR	10	87.6 ± 0.9
B-magnetite	100	86.1 ± 0.9
MAGOR	100	85.9 ± 0.9
B-magnetite	300	76.4 ± 0.8
MAGOR	300	76.1 ± 0.8

The estimated saturation magnetization (M_s) is very high, taking into account that the bulk magnetite Ms is reported to be about 98 emu/g at low temperatures and about 84−88 at 300 K.[36,42,43] The M_s value for the two MNP samples is the same, inside the experimental error, and it reaches the 85% of the bulk M_s (see Table 1). This result can be explained in terms of good crystallization of the particles and reduced surface disorder, as revealed by XRD measurements and TEM observations.[36,44−47] It is important to stress that M_s in maghemite is 20% lower with respect to magnetite one, for nanoparticles having same dimensions,[48] so it is reasonable to suppose that the main phase in our iron oxide nanoparticles is magnetite. The high saturation magnetization is a favorable characteristic of MAGOR nanoparticles that confirms their relevance for applications in drug delivery.[21]

Both samples show small hysteretic behavior: coercivity (H_c) and remanence (M_r) are reported in Tables 2 and 3.

The size distribution affects the behavior of the particles' assembly. In fact, the SPM behavior is stated for particle size

Table 2. Coercivity and Remanence at Different Temperatures for B-Magnetite

	B-magnetite	
temperature (K)	H_c (Oe)	M_r (emu/g)
10	16 (2)	3.7 (6)
100	7 (1)	1.5 (2)
300	1.1 (2)	0.19 (3)

Table 3. Coercivity and Remanence at Different Temperatures for MAGOR

	MAGOR	
temperature (K)	H_c (Oe)	M_r (emu/g)
10	63 (9)	11 (2)
100	27 (4)	5.1 (8)
300	2.4 (4)	0.50 (8)

lower than 25−30 nm,[36] so not all the particles are in the SPM state as put in evidence by hysteresis loops measurements. On the other hand, even if all the particles are not in the SPM state, the values of H_c and M_r are very small, especially at high temperatures. These values are similar to H_c and M_r found for Fe_3O_4 particles in the literature,[36,42] where a SPM-like state is defined in order to underline the low interaction condition at room temperature. Therefore, it is important to stress that the agglomeration of some MNPs, visible in the TEM image of Figure 3a, is not due to the magnetic interaction among particles, which could be a problem for specific medical applications, but more likely to the surface tension of the solvent (used to prepare the samples for TEM observations) during evaporation.

3. CONCLUSIONS

MAGOR, a new nanomaterial containing (R)-9-acetoxystearic acid bound for the first time to magnetite nanoparticles was prepared. The organic coating was made through a synthetic sequence in which a key role was played by APTES, a bidentate linker that reacted with both (R)-9-acetoxystearic acid and nanomagnetite (through silyl groups). 9-HSA was bound to APTES via amide formation (Schotten−Baumann like) after protection as 9-acetoxy derivative. Magnetic iron oxide nanoparticles prior (B-magnetite) and after the coating (MAGOR) were characterized by suitable and complementary techniques. IR and TGA analyses have allowed to evidence the link between nanoparticle and the organic coating and to estimate the upload of the organic material (∼9 wt %).

XRD and TEM measurements have revealed that the upload of the organic material does not influence size, composition, and crystallinity of the MNPs, which are single crystals with dimensions ranging from 10 to 40 nm and a mean value of about 17 nm: apt for drug delivery applications.

Magnetic characterization has evidenced the suitability of the MAGOR nanoparticles for magnetic drug delivery because of (i) their monodomain structure and low magnetic interaction, able to prevent agglomeration at room temperature and (ii) their high magnetization saturation, important to guide the drug to the target site through an external magnetic field.

Thus, the novel material possesses all the necessary properties for being used in magnetically-guided delivery of 9-HSA, a known antiproliferative agent acting selectively against cancer cells. This work paves now the way to

biochemical studies on MAGOR delivery and effects, for example, *in vitro* or through local deposit.

4. EXPERIMENTAL SECTION

4.1. Materials. Iron(III) pentahydrate sulphate ($Fe_2(SO_4)_3 \cdot 5H_2O$, 97%), ammonia (NH_3, 28−30 wt %, d = 0.9 g/cm^3), diethyl ether, ethyl acetate, dichloromethane, toluene, ethanol (95%), vinyl acetate, and lipase acrylic resin from *Candida antarctica* 10,000 U/g (Novozyme 435) were purchased from Sigma-Aldrich. $CDCl_3$ was from Euriso-top (Saint-Aubin, France), iron(II) heptahydrate sulphate ($Fe_2SO_4 \cdot 7H_2O$, 95%) and triethylamine (TEA, 99%) were from Carlo Erba (Italy), and oxalyl chloride was from Alfa Aesar, Thermo Fisher Scientific (Karlsruhe, Germany). Ultrapure UPP water used for magnetite synthesis was obtained with a Milli-Q plus system (Millipore Co., resistivity 18MΩcm). (*R*)-9-Hydroxystearic acid was synthesized from *Dimorphotheca sinuata* L. seeds, as previously described.[27] CH_2Cl_2 was dried by distillation over P_2O_5 and stored under an argon atmosphere. Toluene was dehydrated by distillation under nitrogen on Na/K amalgam and stored under nitrogen on 4 Å molecular sieves.

4.2. Characterization Techniques. *4.2.1. Nuclear Magnetic Resonance.* The NMR spectra (^{1}H, ^{13}C, DEPT) were recorded on Varian spectrometers Gemini 300, Mercury 400 and Inova 600 (Varian, Palo Alto, USA). The frequencies are given in Hz, and the chemical shift is given in ppm using the chemical shift of the solvent $CDCl_3$ as the reference (7.26 and 77.0 ppm for ^{1}H and ^{13}C NMR, respectively).

4.2.2. IR Spectra. IR spectra were recorded using a Fourier transform spectrophotometer PerkinElmer FT-IR spectrometer Spectrum Two in the 4000−500 cm^{-1} wavelength range, using a NaCl cell for liquid samples, whereas the spectra of solid samples were recorded using an Universal ATR accessory.

4.2.3. Mass Spectra. ESI-MS spectra were recorded on a mass spectrometry WATERS 2Q 4000.

4.2.4. pH Measurements. The pH-measures were carried out on a AMEL334-B, calibrated with standard solutions at pH = 7 and pH = 9.

4.2.5. Thermogravimetric Analyses. They were performed using a PerkinElmer TGA-7 with a heating ramp from 37 to 700 °C at a rate of 10 °C/min, under air flux.

4.2.6. X-ray Diffractometry. Powder X-ray diffractometry was carried out using a Panalytical X'Pert Pro (Cu Kα radiation, λ = 0.154 nm, 40 mA, 40 kV). The peak broadening was used to evaluate the crystal size (τ_{hkl}), which was calculated from the width at half maximum intensity ($\beta_{1/2}$) using the Scherrer equation (eq 3)[33]

$$\tau_{hkl} = \frac{k\lambda}{\beta_{1/2}\cos\theta} \tag{3}$$

where λ is the wavelength, θ the diffraction angle, and K a constant depending on crystal habit (chosen as 1). For crystal size calculation, the most intense reflection for magnetite was taken into consideration, that is, peak (311).

4.2.7. Transmission Electron Microscopy. The size and inner structure of the NPs were investigated by TEM techniques using a Philips CM200 microscope operating at 200 kV and equipped with a LaB6 filament. For TEM observations, a small quantity of NPs was dispersed in ethanol and subjected to ultrasonic agitation for approximately one min. A drop of the suspension was deposited on a commercial TEM grid covered with a thin carbon film; finally, the grid is kept in air until complete evaporation of the ethanol.

4.2.8. Magnetic Measurements. Magnetic measurements were performed by means of a Quantum Design PPMS ac/dc Magnetometry System (ACMS). The measurements are based on the mutual-inductance technique using the ACMS coil set and electronics. Magnetization data as a function of temperature have been measured till 30 kOe. ZFC and FC protocols have been applied to evaluate the temperature dependence of the magnetization.[35,41] The ZFC−FC magnetization measurements have been performed at first by cooling the sample starting from room temperature to 2 K in zero magnetic field. A small static magnetic field of 100 Oe was then applied, and the ZFC measurement was performed during the warmup from 2 to 350 K. The FC measurement was recorded, as a function of the temperature, while the sample was cooled down to 2 K. Hysteresis loops have been performed at 10, 100, and 300 K till 10 kOe to evaluate the coercivity and remanence as a function of the temperature.

4.3. Synthesis of the Organic Coating. *4.3.1. Synthesis of (R)-9-Acetoxyoctadecanoic Acid (2).* To a mixture of (*R*)-9-hydroxystearic acid (0.60 g, 2.0 mmol) and vinyl acetate (10 mL), diethyl ether was added until dissolution of the solid (about 20 mL). Novozyme 435 (0.630 g) was added, and the mixture was stirred at 30 °C for 5 days. The suspension was filtered through a Gooch funnel, and the enzyme was washed with diethyl ether and ethyl acetate. Evaporation of the combined organic phases afforded acetylated product (0.66 g, 1.9 mmol, 97% yield). ^{1}H NMR (600 MHz, $CDCl_3$, 298 K): δ, ppm: 4.85 (qt, J = 5.8 Hz, 1H, CHOH), 2.34 (t, J = 7.4 Hz, 2H, CH_2COOH), 2.04 (s, 3H, CH_3CO), 1.63 (qt, J = 7.3 Hz, 2H, CH_2CH_2COOH), 1.55−1.45 (m, 4H), 1.37−1.20 (m, 22H, remaining CH_2 chain), 0.88 (t, J = 6.9 Hz, 3H, CH_3); ^{13}C NMR (150.8 MHz, $CDCl_3$, 298 K): δ, ppm: 179.6, 171.0, 74.4, 34.1, 34.03, 33.9, 31.8, 29.5 (2 signals overlapped), 29.26 (2 signals overlapped), 29.1, 28.9, 25.20, 25.19, 24.6, 22.7, 21.3, 14.1; ESI-MS$^+$ (m/z): 365 [M + Na]$^+$, 381 [M + K]$^+$; ESI-MS$^-$ (m/z): 341 [M − H]$^-$; IR (ν, cm^{-1}): 3428, 2958, 2925, 2856, 1735, 1705, 1646, 1462, 1373, 1242, 1027.

4.3.2. Synthesis of (R)-1-Chloro-1-oxooctadecan-9-yl Acetate (3). Into a three-necked round-bottom flask and under an argon atmosphere, (*R*)-9-acetoxyoctadecanoic acid (300 mg, 0.00088 mol) was dissolved in anhydrous CH_2Cl_2 (10 mL). Oxalyl chloride (0.077 mL, 0.00088 mol) was added to the solution, and the mixture was stirred for 24 h at room temperature. The reaction course was monitored by ^{1}H NMR spectroscopy. When it resulted complete, the solvent was removed and the oil obtained was used without purification. ^{1}H NMR (400 MHz, $CDCl_3$, 298 K): δ, ppm: 4.85 (qt, J = 5.9 Hz, 1H, CHOH), 2.88 (t, J = 7.3 Hz, 2H, CH_2COOH), 2.04 (s, 3H, CH_3CO), 1.70 (qt, J = 7.4 Hz, 2H, CH_2CH_2COOH), 1.55−1.45 (m, 4 H), 1.39−1.19 (m, 22 H), 0.88 (t, J = 7.0 Hz, 3H, CH_3); ^{13}C NMR (100.5 MHz, $CDCl_3$, 298 K): δ, ppm: 173.8, 171.0, 74.3, 53.4, 47.1, 34.1, 34.0, 31.9, 29.5 (2 signals overlapped), 29.3, 29.2, 28.9, 28.3, 25.3, 25.2, 25.0, 22.7, 21.3, 14.1; IR (ν, cm^{-1}, neat): 2928, 2858, 1791, 1721, 1378, 1266, 1019.

4.3.3. Synthesis of (R)-1-Oxo-1-((3-(triethoxysilyl)propyl)-amino)octadecan-9-yl Acetate (4). Triethylamine (0.122 mL, 0.00088 mol) and APTES (0.20 mL, 0.00088 mol) were added to a solution of **3** (0.00088 mol) in CH_2Cl_2 (10 mL), and the mixture was stirred for 3 h at room temperature. The reaction was monitored by ^{1}H NMR spectroscopy until it resulted

complete. The solvent was removed under inert atmosphere to avoid exposure to air, the solvent was removed, and the residue was used without purification. ^{1}H NMR (600 MHz, CDCl$_3$, 298 K): δ, ppm: 4.76 (qt, J = 6.03 Hz, 1H, CHOH), 3.73 (q, J = 7.1 Hz, 6H, CH$_2$OSi), 3.16 (q, J = 6.4 Hz, 2H, CH$_2$NH), 2.08 (t, J = 7.6 Hz, 2H, CH$_2$COOH), 1.90 (s, 3H, CH$_3$CO), 1.57−1.46 (m, 2 H), 1.47−1.37 (m, 4 H), 1.22−1.10 (m + t, 24H + 9H, aliphatic chain + CH$_3$CH$_2$OSi), 0.77 (t, J = 7.0 Hz, 3H, CH$_3$), 0.53 (t, J = 8.1 Hz, 2H, CH$_2$Si); ^{13}C NMR (150.8 Hz, CDCl$_3$, 298 K): δ, ppm: 172.9, 170.8, 74.2, 58.2, 45.6, 41.6, 36.6, 33.92, 33.87, 31.7, 29.3 (2 signals overlapped), 29.10, 29.08, 29.01 25.6, 25.11, 25.06, 22.7, 22.5, 21.1, 18.1, 13.9, 8.5; ESI-MS$^+$ (m/z): 568 [M + Na]$^+$, 584 [M + K]$^+$; IR (ν, cm^{-1}, neat): 3448, 2930, 2859, 2416, 2248, 2212, 1717, 1662, 1520, 1465, 1387, 1371, 1261, 1103, 1077.

4.3.4. Preparation of Bare Magnetite (Fe$_3$O$_4$) Nanoparticles (B-Magnetite). The synthesis of bare magnetite nanoparticles was carried out following a previous protocol.[33,49] Into a three-necked round-bottom flask, FeSO$_4$·7H$_2$O (2.788 g, 0.010 mol) and Fe$_2$(SO$_4$)$_3$·5H$_2$O (5.131 g, 0.010 mol) were dissolved in 100 mL of water Milli-Q purity grade, and the solution was degassed with three vacuum/nitrogen purging cycles. An excess of ammonia (13.0 mL, 0.200 mol) was added dropwise monitoring the pH of the mixture until to pH = 10.4. The black suspension was stirred for 2 h at 60 °C and cooled and allowed to stand. MNPs were separated from the supernatant solution using an external magnetic bar and thoroughly washed with water and ethanol, dried at 60 °C, and kept under vacuum for 12 h at 50 °C. The final product (2.220 g, 96% yield) was stored under an argon atmosphere.

4.3.5. Functionalization of B-Magnetite with 4. Dry toluene (10 mL), MNPs (B-magnetite, 205 mg, 0.88 mmol), and Et$_3$N (10 μL, 0.072 mmol) were added to the crude amide **4** (0.88 mmol). The suspension was vigorously stirred for 24 h at 60 °C and then maintained at 100 °C for 1 h. The solvent was removed using Magnetic bar's technique described for the synthesis of MNPs (sub-section 4.3.4), and then, the product was washed with dry toluene. (*R*)-1-Oxo-1-((3-(triethoxysilyl)-propyl)amino)octadecan-9-yl acetate-coated MNPs, hereinafter indicated as MAGOR, were first dried in an oven for 12 h (70 °C) and then kept under vacuum for 12 h. IR analysis confirmed the presence of characteristic bands of organic groups: IR (ν, cm^{-1}): 2930.4, 1735.2, 1659.8, 1478.8, 1121.4, and 1031.7.

ASSOCIATED CONTENT

Ⓢ Supporting Information

The Supporting Information is available free of charge at https://pubs.acs.org/doi/10.1021/acsomega.0c00163.

Copies of ^{1}H NMR and ^{13}C NMR spectra of compounds **2−4**, IR spectra of B-magnetite and MAGOR, and TEM bright field images of MAGOR nanoparticles (PDF)

AUTHOR INFORMATION

Corresponding Authors

Carla Boga − *Department of Industrial Chemistry "Toso Montanari", University of Bologna, 40136 Bologna, Italy;* Ⓞ orcid.org/0000-0003-2851-8939; Email: carla.boga@unibo.it

Daniele Rinaldi − *Department of Materials, Environmental Sciences and Urban Planning, Università Politecnica delle Marche, 60131 Ancona, Italy;* Ⓞ orcid.org/0000-0003-1676-9044; Email: d.rinaldi@staff.univpm.it

Authors

Gabriele Micheletti − *Department of Industrial Chemistry "Toso Montanari", University of Bologna, 40136 Bologna, Italy;* Ⓞ orcid.org/0000-0001-9746-2356

Dario Telese − *Department of Industrial Chemistry "Toso Montanari", University of Bologna, 40136 Bologna, Italy*

Maria Cristina Cassani − *Department of Industrial Chemistry "Toso Montanari", University of Bologna, 40136 Bologna, Italy;* Ⓞ orcid.org/0000-0002-7155-8744

Elisa Boanini − *Department of Chemistry "G. Ciamician", University of Bologna, 40126 Bologna, Italy;* Ⓞ orcid.org/0000-0003-3754-0273

Patrizia Nitti − *Department of Chemical and Pharmaceutical Sciences, University of Trieste, 34127 Trieste, Italy*

Barbara Ballarin − *Department of Industrial Chemistry "Toso Montanari", University of Bologna, 40136 Bologna, Italy;* Ⓞ orcid.org/0000-0003-3698-2352

Alberto Ghirri − *Istituto Nanoscienze—CNR, 41125 Modena, Italy;* Ⓞ orcid.org/0000-0001-7316-3765

Gianni Barucca − *Department of Materials, Environmental Sciences and Urban Planning, Università Politecnica delle Marche, 60131 Ancona, Italy;* Ⓞ orcid.org/0000-0002-7368-6264

Complete contact information is available at:
https://pubs.acs.org/10.1021/acsomega.0c00163

Author Contributions

The manuscript was written through contributions of all authors. All authors have given approval to the final version of the manuscript.

Notes

The authors declare no competing financial interest.

ACKNOWLEDGMENTS

ABBREVIATIONS

APTES, (3-aminopropyl)triethoxysilane; B-magnetite, bare magnetite (Fe$_3$O$_4$) nanoparticles; 9-HSA, (*R*)-9-hydroxystearic acid; MAGOR, (*R*)-1-oxo-1-((3-(triethoxysilyl)propyl)-amino)octadecan-9-yl acetate-coated magnetic nanoparticles; MNPs, magnetic nanoparticles; MRI, magnetic resonance imaging; NPs, nanoparticles; PET, positron emission tomography; SPM, superparamagnetic

REFERENCES

(1) Ngomsik, A.-F.; Bee, A.; Draye, M.; Cote, G.; Cabuil, V. Magnetic Nano- and Microparticles for Metal Removal and Environmental Applications: A Review. *C. R. Chim.* **2005**, *8*, 963−970.

(2) Saharan, P.; Chaudhary, G. R.; Mehta, S. K.; Umar, A. Removal of water contaminants by iron oxide nanomaterials. *J. Nanosci. Nanotechnol.* **2014**, *14*, 627−643.

(3) Sharma, M.; Kalita, P.; Senapati, K. K.; Ankit Garg, A. Study on Magnetic Materials for Removal of Water Pollutants. In *Emerging Pollutants-Some Strategies for the Quality Preservation of Our Environment*; Soloneski, S., Larramendy, M. L., Eds.; IntechOpen: London, 2018; pp 61−78.

(4) Chenthamara, D.; Subramaniam, S.; Ramakrishnan, S. G.; Krishnaswamy, S.; Essa, M. M.; Lin, F.-H.; Qoronfleh, M. W. Therapeutic efficacy of nanoparticles and routes of administration. *Biomater. Res.* **2019**, *23*, 20.

(5) Gobbo, O. L.; Sjaastad, K.; Radomski, M. W.; Volkov, Y.; Prina-Mello, A. Magnetic Nanoparticles in Cancer Theranostics. *Theranostics* **2015**, *5*, 1249−1263.

(6) Yu, M. K.; Jeong, Y. Y.; Park, J.; Park, S.; Kim, J. W.; Min, J. J.; Kim, K.; Jon, S. Drug-Loaded Superparamagnetic Iron Oxide Nanoparticles for Combined Cancer Imaging and Therapy In Vivo. *Angew. Chem., Int. Ed.* **2008**, *47*, 5362−5365.

(7) Morais, P. C. Nanoparticulated Magnetic Drug Delivery Systems: Preparation and Magnetic Characterization. *J. Phys.: Conf. Ser.* **2010**, *217*, 012091.

(8) Williams, H. M. The Application of Magnetic Nanoparticles in the Treatment and Monitoring of Cancer and Infectious Diseases. *Biosci. Horiz.* **2017**, *10*, hzx009.

(9) Montalto, L.; Paone, N.; Scalise, L.; Rinaldi, D. A photoelastic measurement system for residual stress analysis in scintillating crystals by conoscopic imaging. *Rev. Sci. Instrum.* **2015**, *86*, 063102.

(10) Scalise, L.; Rinaldi, D.; Davì, F.; Paone, N. Measurement of ultimate tensile strength and Young modulus in LYSO scintillating crystals. *Nucl. Instrum. Methods Phys. Res., Sect. A* **2011**, *654*, 122−126.

(11) Mengucci, P.; André, G.; Auffray, E.; Barucca, G.; Cecchi, C.; Chipaux, R.; Cousson, A.; Davì, F.; Di Vara, N.; Rinaldi, D.; Santecchia, E. Structural, mechanical and light yield characterisation of heat treated LYSO:Ce single crystals for medical imaging applications. *Nucl. Instrum. Methods Phys. Res., Sect. A* **2015**, *785*, 110−116.

(12) Rinaldi, D.; Ciriaco, A.; Lebeau, M.; Paone, N. Quality control on pre-serial Bridgman production of PbWO₄ scintillating crystals by means of photoelasticity. *Nucl. Instrum. Methods Phys. Res., Sect. A* **2010**, *615*, 254−258.

(13) Arruebo, M.; Fernández-Pacheco, R.; Ibarra, M. R.; Santamaría, J. Magnetic Nanoparticles for Drug Delivery. *Nano Today* **2007**, *2*, 22−32.

(14) Derfus, A. M.; von Maltzahn, G.; Harris, T. J.; Duza, T.; Vecchio, K. S.; Ruoslahti, E.; Bhatia, S. N. Remotely Triggered Release from Magnetic Nanoparticles. *Adv. Mater.* **2007**, *19*, 3932−3936.

(15) Kohler, N.; Sun, C.; Fichtenholtz, A.; Gunn, J.; Fang, C.; Zhang, M. Methotrexate-immobilized Poly(ethylene glycol) Magnetic Nanoparticles for MR Imaging and Drug Delivery. *Small* **2006**, *2*, 785−792.

(16) Jain, T. K.; Morales, M. A.; Sahoo, S. K.; Leslie-Pelecky, D. L.; Labhasetwar, V. Iron Oxide Nanoparticles for Sustained Delivery of Anticancer Agents. *Mol. Pharmacol.* **2005**, *2*, 194−205.

(17) Wang, X.; Zhang, R.; Wu, C.; Dai, Y.; Song, M.; Gutmann, S.; Gao, F.; Lv, G.; Li, J.; Li, X.; Guan, Z.; Fu, D.; Chen, B. The Application of Fe₃O₄ Nanoparticles in Cancer Research: A New Strategy to Inhibit Drug Resistance. *J. Biomed. Mater. Res., Part A* **2007**, *80*, 852−860.

(18) Nuzhina, J. V.; Shtil, A. A.; Prilepskii, A. Y.; Vinogradov, V. V. Preclinical Evaluation and Clinical Translation of Magnetite-Based Nanomedicines. *J. Drug Deliv. Sci. Technol.* **2019**, *54*, 101282.

(19) Ehsani, M. H.; Esmaeili, S.; Aghazadeh, M.; Kameli, P.; Karimzadeh, I. Magnetic Evaluation of the Nanoparticles Coated with Polyvinylpyrrolidone and Polyvinyl Chloride Nanoparticles Synthesized by Electro-deposition Method for Hyperthermia Application. *J. Supercond. Novel Magn.* **2019**, *32*, 2021−2030.

(20) Tran, N.; Webster, T. J. Magnetic nanoparticles: Biomedical Applications and Challenges. *J. Mater. Chem.* **2010**, *20*, 8760−8767.

(21) Gupta, A. K.; Gupta, M. Synthesis and Surface Engineering of Iron Oxide Nanoparticles for Biomedical Applications. *Biomaterials* **2005**, *26*, 3995−4021.

(22) Piñeiro, Y.; Vargas, Z.; Rivas, J.; López-Quintela, M. A. Iron Oxide Based Nanoparticles for Magnetic Hyperthermia Strategies in Biological Applications. *Eur. J. Inorg. Chem.* **2015**, 4495−4509.

(23) Bedanta, S.; Kleemann, W. Supermagnetism. *J. Phys. D Appl. Phys.* **2009**, *42*, 013001.

(24) Calonghi, N.; Cappadone, C.; Pagnotta, E.; Farruggia, G.; Buontempo, F.; Boga, C.; Brusa, G. L.; Santucci, M. A.; Masotti, L. 9-Hydroxystearic Acid Upregulates p21ᵂᴬᶠ¹ in HT29 Cancer Cells. *Biochem. Biophys. Res. Commun.* **2004**, *314*, 138−142.

(25) Calonghi, N.; Pagnotta, E.; Parolin, C.; Molinari, C.; Boga, C.; Dal Piaz, F.; Brusa, G. L.; Santucci, M. A.; Masotti, L. Modulation of Apoptotic Signalling by 9-Hydroxystearic Acid in Osteosarcoma Cells. *Biochim. Biophys. Acta, Mol. Cell Biol. Lipids* **2007**, *1771*, 139−146.

(26) Calonghi, N.; Cappadone, C.; Pagnotta, E.; Boga, C.; Bertucci, C.; Fiori, J.; Tasco, G.; Casadio, R.; Masotti, L. Histone Deacetylase 1: A Target of 9-Hydroxystearic Acid in the Inhibition of Cell Growth in Human Colon Cancer. *J. Lipid Res.* **2005**, *46*, 1596−1603.

(27) Parolin, C.; Calonghi, N.; Presta, E.; Boga, C.; Caruana, P.; Naldi, M.; Andrisano, V.; Masotti, L.; Sartor, G. Mechanism and Stereoselectivity of HDAC I Inhibition by (R)-9-hydroxystearic Acid in Colon Cancer. *Biochim. Biophys. Acta* **2012**, *1821*, 1334−1340.

(28) Busi, A.; Aluigi, A.; Guerrini, A.; Boga, C.; Sartor, G.; Calonghi, N.; Sotgiu, G.; Posati, T.; Corticelli, F.; Fiori, J.; Varchi, G.; Ferroni, C. Unprecedented Behavior of (9R)-9-hydroxystearic Acid Loaded Keratin Nanoparticles on Cancer Cell Cycle. *Mol. Pharm.* **2019**, *16*, 931−942.

(29) Boanini, E.; Torricelli, P.; Boga, C.; Micheletti, G.; Cassani, M. C.; Fini, M.; Bigi, A. (9R)-9-Hydroxystearate-Functionalized Hydroxyapatite as Anti-Proliferative and Cytotoxic Agent towards Osteosarcoma Cells. *Langmuir* **2016**, *32*, 188−194.

(30) Boanini, E.; Cassani, M.; Rubini, K.; Boga, C.; Bigi, A. (9R)-9-Hydroxystearate-Functionalized Anticancer Ceramics Promote Loading of Silver Nanoparticles. *Nanomaterials* **2018**, *8*, 390.

(31) Yamaura, M.; Camilo, R. L.; Sampaio, L. C.; Macêdo, M. A.; Nakamura, M.; Toma, H. E. Preparation and Characterization of (3-aminopropyl) triethoxysilane-coated Magnetite Nanoparticles. *J. Magn. Magn. Mater.* **2004**, *279*, 210−217.

(32) Boga, C.; Micheletti, G.; Orlando, I.; Strocchi, E.; Vitali, B.; Verardi, L.; Sartor, G.; Calonghi, N. New Hybrids with 2-aminobenzothiazole and Azelayl Scaffolds: Synthesis, Molecular Docking and Biological Evaluation. *Curr. Org. Chem.* **2018**, *22*, 1649−1660.

(33) Ballarin, B.; Cassani, M. C.; Nanni, D.; Parise, C.; Barreca, D.; Carraro, G.; Riminucci, A.; Bergenti, I.; Morandi, V.; Migliori, A.; Boanini, E. Structure, morphology and magnetic properties of Au/Fe₃O₄ nanocomposites fabricated by a soft aqueous route. *Ceram. Int.* **2019**, *45*, 449−456.

(34) Dehsari, H. S.; Ksenofontov, V.; Möller, A.; Jakob, G.; Asad, K. Determining Magnetite/Maghemite Composition and Core−Shell Nanostructure from Magnetization Curve for Iron Oxide Nanoparticles. *J. Phys. Chem. C* **2018**, *122*, 28292−28301.

(35) Bedanta, S.; Petracic, O.; Kleemann, W. *Supermagnetism in Handbook of Magnetic Materials*, 1st ed.; Buschow, K. H. J., Ed.; Elsevier: Oxford, 2015; Vol. 23, pp 1−83.

(36) Kolen'Ko, Y. V.; Bañobre-López, M.; Rodríguez-Abreu, C.; Carbó-Argibay, E.; Sailsman, A.; Piñeiro-Redondo, Y.; Cerqueira, M. F.; Petrovykh, D. Y.; Kovnir, K.; Lebedev, O. I.; Rivas, J. Large-scale Synthesis of Colloidal Fe₃O₄ Nanoparticles Exhibiting High Heating Efficiency in Magnetic Hyperthermia. *J. Phys. Chem. C* **2014**, *118*, 8691−8701.

(37) Peddis, D.; Rinaldi, D.; Ennas, G.; Scano, A.; Agostinelli, E.; Fiorani, D. Superparamagnetic Blocking and Superspin-glass Freezing in Ultra Small δ-(Fe₀.₆₇Mn₀.₃₃)OOH Particles. *Phys. Chem. Chem. Phys.* **2012**, *14*, 3162−3169.

(38) Lavorato, G.; Winkler, E.; Ghirri, A.; Lima, E., Jr.; Peddis, D.; Troiani, H. E.; Fiorani, D.; Agostinelli, E.; Rinaldi, D.; Zysler, R. D. Exchange bias and surface effects in bimagnetic CoO-core/Co₀.₅Ni₀.₅Fe₂O₄ -shell nanoparticles. *Phys. Rev. B* **2016**, *94*, 054432.

(39) Muscas, G.; Concas, G.; Cannas, C.; Musinu, A.; Ardu, A.; Orrù, F.; Fiorani, D.; Laureti, S.; Rinaldi, D.; Piccaluga, G.; Peddis, D. Magnetic Properties of Small Magnetite Nanocrystals. *J. Phys. Chem. C* **2013**, *117*, 23378−23384.

(40) Lee, J. S.; Cha, J. M.; Yoon, H. Y.; Lee, J. K.; Kim, Y. K. Magnetic Multi-granule Nanoclusters: A Model System that Exhibits Universal Size Effect of Magnetic Coercivity. *Sci. Rep.* **2015**, *5*, 12135.

(41) Peddis, D.; Cannas, C.; Musinu, A.; Ardu, A.; Orrù, F.; Fiorani, D.; Laureti, S.; Rinaldi, D.; Muscas, G.; Concas, G.; Piccaluga, G. Beyond the Effect of Particle Size: Influence of $CoFe_2O_4$ Nanoparticle Arrangements on Magnetic Properties. *Chem. Mater.* **2013**, *25*, 2005−2013.

(42) Caruntu, D.; Caruntu, G.; O'Connor, C. J. Magnetic Properties of Variable-sized Fe_3O_4 Nanoparticles Synthesized from Non-aqueous Homogeneous Solutions of Polyols. *J. Phys. D: Appl. Phys.* **2007**, *40*, 5801−5809.

(43) Bianco, L. D.; Lesci, I. G.; Fracasso, G.; Barucca, G.; Spizzo, F.; Tamisari, M.; Scotti, R.; Ciocca, L. Synthesis of Nanogranular Fe_3O_4/biomimetic Hydroxyapatite for Potential Applications in Nano-medicine: Structural and Magnetic Characterization. *Mater. Res. Express* **2015**, *2*, 065002.

(44) Mitra, A.; Mohapatra, J.; Meena, S. S.; Tomy, C. V.; Aslam, M. Verwey Transition in Ultrasmall-sized Octahedral Fe_3O_4 Nano-particles. *J. Phys. Chem. C* **2014**, *118*, 19356−19362.

(45) Goya, G. F.; Berquó, T. S.; Fonseca, F. C.; Morales, M. P. Static and Dynamic Magnetic Properties of Spherical Magnetite Nano-particles. *J. Appl. Phys.* **2003**, *94*, 3520−3528.

(46) Muthukumaran, T.; Philip, J. Effect of Phosphate and Oleic Acid Capping on Structure, Magnetic Properties and thermal Stability of Iron Oxide Nanoparticles. *J. Alloys Compd.* **2016**, *689*, 959−968.

(47) Varvaro, G.; Testa, A. M.; Agostinelli, E.; Fiorani, D.; Laureti, S.; Springer, F.; Brombacher, C.; Albrecht, M.; Del Bianco, L.; Barucca, G.; Mengucci, P.; Rinaldi, D. Study of microstructure and magnetization reversal mechanism in granular $CoCrPt:SiO_2$ films of variable thickness. *Mater. Chem. Phys.* **2013**, *141*, 790−796.

(48) Kucheryavy, P.; He, J.; John, V. T.; Maharjan, P.; Spinu, L.; Goloverda, G. Z.; Kolesnichenko, V. L. Superparamagnetic Iron Oxide Nanoparticles with Variable Size and an Iron Oxidation State as Prospective Imaging Agents. *Langmuir* **2013**, *29*, 710−716.

(49) Baig, R. B. N.; Varma, R. S. A facile One-pot Synthesis of Ruthenium Hydroxide Nanoparticles on Magnetic Silica: Aqueous Hydration of Nitriles to Amides. *Chem. Commun.* **2012**, *48*, 6220−6222.